Available online at www.sciencedirect.com

ScienceDirect

journal homepage: www.elsevier.com/locate/he

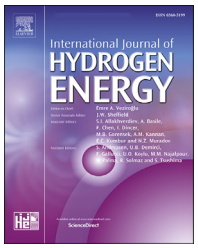

Photocatalytic hydrogen production by biomimetic indium sulfide using *Mimosa pudica* leaves as template

Omar A. Carrasco-Jaim [a], *Ruben Ahumada-Lazo* [b], *Pip C.J. Clark* [b,1], *Christian Gómez-Solis* [a,*,2], *Simon M. Fairclough* [c], *Sarah J. Haigh* [c], *Marina A. Leontiadou* [b,3], *Karsten Handrup* [d,4], *Leticia M. Torres-Martínez* [a], *Wendy R. Flavell* [b]

[a] *Departamento de Ecomateriales y Energía, Facultad de Ingeniería Civil, Universidad Autónoma de Nuevo León, Av. Universidad S/N Ciudad Universitaria, San Nicolás de Los Garza, Nuevo León, 66455, Mexico*

[b] *School of Physics and Astronomy and the Photon Science Institute, the University of Manchester, Manchester M13 9PL, United Kingdom*

[c] *School of Materials, The University of Manchester, Manchester M13 9PL, United Kingdom*

[d] *MaxLab, Ole Römers Väg, 1 223 63 Lund, Sweden*

ARTICLE INFO

Article history:
Received 13 May 2018
Received in revised form
16 November 2018
Accepted 5 December 2018
Available online 5 January 2019

Keywords:
$In_{2.77}S_4$
Template-assisted hydrothermal
Photocatalytic hydrogen production
XPS analysis

ABSTRACT

Biomimetic sulfur-deficient indium sulfide ($In_{2.77}S_4$) was synthesized by a template-assisted hydrothermal method using leaves of *Mimosa pudica* as a template for the first time. The effect of this template in modifying the morphology of the semiconductor particles was determined by physicochemical characterization, revealing an increase in surface area, decrease in microsphere size and pore size and an increase in pore volume density in samples synthesized with the template. X-ray photoelectron spectroscopy (XPS) analysis showed the presence of organic sulfur (S–O/S–C/S–H) and sulfur oxide species (–SO_2, SO_3^{2-}, SO_4^{2-}) at the surface of the indium sulfide in samples synthesized with the template. Biomimetic indium sulfide also showed significant amounts of Fe introduced as a contaminant present on the *Mimosa pudica* leaves. The presence of these sulfur and iron species favors the photocatalytic activity for hydrogen production by their acting as a sacrificial reagent and promoting water oxidation on the surface of the templated particles, respectively. The photocatalytic hydrogen production rates over optimally-prepared biomimetic indium sulfide and indium sulfide synthesized without the organic template were 73 and 22 μmol g^{-1}, respectively, indicating an improvement by a factor of three in the templated sample.

* *Corresponding author.*
E-mail address: lienquidremo@gmail.com (C. Gómez-Solis).
[1] Present address: Institute for Solar Fuels Helmholtz-Zentrum Berlin fur Materialien und Energie GmbH Hahn-Meitner Platz 1, D-14109 Berlin, Germany.
[2] Present address: División de Ciencias e Ingenierías, Universidad de Guanajuato, Campus León, Loma del Bosque 103, Colonia Lomas del Campestre, León, Guanajuato, 37150, México.
[3] Present address: Joule Physics Laboratory, School of Computing, Science and Engineering, University of Salford, Manchester M5 4WT, United Kingdom.
[4] Present address: Department of Physics and Astronomy, Aarhus University, Ny Munkegade 120, DK-8000 Aarhus C, Denmark.
https://doi.org/10.1016/j.ijhydene.2018.12.043

Introduction

Hydrogen has emerged as a next-generation energy carrier, and in recent years photocatalytic water splitting using solar energy has been studied as a potential method for sustainable hydrogen production. Since Fujishima and Honda demonstrated that photocatalytic water splitting can be achieved using a photoelectrochemical cell containing a TiO_2 semiconductor anode, a large number of semiconductors have been developed for this purpose. Unfortunately, most of them are wide band gap semiconductors and only active under UV light irradiation [1–5]. To make the most of the abundant solar spectrum, the development of visible-light-driven photocatalysts is needed. Sulfides are attractive candidates due to their suitable band gaps and good catalytic activities for hydrogen production, with CdS being widely studied as a significant sulfide in this regard [6–9]. However, its photocatalytic efficiency is low due to recombination of charge carriers, and it is not stable under light irradiation because it suffers from photo-corrosion [10]. In_2S_3, a typical III–VI group chalcogenide with a band gap of 2.0–2.2 eV, has also been thoroughly investigated as a visible-light and non-toxic photocatalyst due to its stable chemical composition and high photoconductivity, properties that also make it useful for applications in photovoltaic solar cells [11–13]. There are three different crystalline structures of In_2S_3: α-In_2S_3, β-In_2S_3, or γ-In_2S_3, can be formed depending on the growth temperature. The β-In_2S_3 phase (typically sulfur-deficient $In_{2.77}S_4$) is the most stable structural form with a cubic or tetragonal structure [14]. Its structure is related to a spinel lattice with the cation vacancies located on either the octahedral or tetrahedral sites. The sulfur-deficient phase can be interpreted as a quasi-ternary compound formula: (In_{1-x}) $(In_2)S_4$, which consists of a unit cell made of In atoms, S atoms and S vacancies [15,16].

Among the many different methods used to process and synthesize inorganic materials, hydrothermal synthesis presents several advantages over more conventional techniques, such as, energy saving and cost effectiveness, simplicity, higher purity products, higher reaction rates, better nucleation control and better control of size and shape [17]. Moreover, desired morphologies can be obtained by using different synthetic strategies, like varying reaction temperature and time, or the incorporation of organic additives and templates to impart structural features. This allows the preparation of highly ordered low-dimensional arrays with morphologies directly determined by the templates [17–20]. Indium sulfide has been synthesized by the hydrothermal method, varying different parameters such as, reaction time, temperature, precursor reagents and additives or templates, with the aim of optimizing its photocatalytic activity for hydrogen evolution or the oxidation of different modelled water pollutants [21–25]. In these studies it was found that only the cubic crystal structure shows photocatalytic activity, while the tetragonal structure does not. Moreover, better activities were found with morphologies favoring the exposure of the (311) plane, which is more active for the photodegradation of dyes than the other planes of this structure [22,23]. Additionally, coupling with other materials such as In_2O_3 and $In(OH)_3$ that induce charge separation, and the design of architectures that enhance light absorption have been demonstrated to improve the photocatalytic performance of indium sulfide [24,25].

Many approaches have been developed to improve absorption of light in photocatalysis, such as doping with noble, transition or non-metals [26–28], and also adopting novel morphology designs. Interestingly, nature creates a diversity of biological structures and species that are currently used as templates to synthesize functional materials [29,30], such as bacteria, pollen grains, butterfly wings, diatoms, stems and leaves [31–37]. Plant leaves are a synergy of intricate structures in which light harvesting, photoinduced charge separation, and catalysis modules combine to perform photosynthesis, capturing the solar energy and splitting water into oxygen and hydrogen (in the form of reducing equivalents) [38,39]. Thus, coupling the leaf-like hierarchical structure onto the electronic structure of a semiconductor may offer a route to the development of new materials for solar energy harvesting and conversion. Based on this concept, we describe a simple and cost-effective method for the controlled synthesis of indium sulfide via a biomimetic method using a template-assisted hydrothermal process. The *Mimosa pudica* leaf was selected as the template because of its microstructure, naturally adapted for the efficient absorption of light (as is evident from its well-known sensitivity to sun light [40,41]), a feature that may be transferrable to the biomimetic material by adopting its morphology to increase light harvesting [42]. This microstructure has recently inspired other designs, like pressure sensors and self-organizing materials for applications in microfluidics, biosensors and water purification systems [43,44]. Moreover, extract from *Mimosa pudica* leaves and flowers is becoming a popular reducing and capping agent (or bio-template) and has already been used in the green synthesis of Ni, Co, Cu, Au, Ag, Fe and ZnO nanoparticles as well as for $CaSiO_3:Pr^{3+}$ and $CaSiO_3:Sm^{3+}$ nanophosphors [45–50].

Experimental

Synthesis of biomimetic indium sulfide by a template-assisted hydrothermal method

Mimosa pudica leaves were collected and washed first with ethanol in a sonicated bath for 15 min, and then with deionized water. The leaves were dried in air for 48 h, pulverized in an agate mortar and used as the template. The proper amount (see below) of indium acetate was dissolved in 40 mL of deionized water in a beaker and 2 mL of sulfuric acid (1:10) was added to adjust the pH to around 2 under stirring. Citric acid (0.2 g) was used as stabilizer agent in the reaction. Finally, thioacetamide and the treated *Mimosa pudica* leaves were added into the solution. In order to evaluate the effect of the amount of template in the synthesis, three weight ratios (indium acetate: *Mimosa pudica*); 2:1, 1:1 and 1:2 were used (referred to as S1, S2 and S3, respectively). Then, the reaction mixture was transferred into a Teflon liner, sealed in a stainless steel autoclave and maintained at 150 °C for 24 h. After cooling to room temperature, the precipitate obtained was vacuum filtered, washed with deionized water several times and calcined at 400 °C for 2 h under a

nitrogen atmosphere. As a comparison, indium sulfide powder was synthesized under the same conditions (including calcination) without the template, (denoted as S0). Additionally, two control samples containing 0.1 and 1 atomic percent of Fe were prepared by adding iron acetylacetonate to evaluate the influence of Fe on in the hydrogen production activity.

Characterization

The crystal structure was determined by X-ray powder diffraction (XRD) with a D8 Advance diffractometer using Cu Kα radiation (λ = 1.5418 Å). The morphology was observed by scanning electron microscopy (SEM) using a JEOL JSM-6490-LV microscope adapted with an energy dispersive X-ray spectroscopy (EDS) system for the semi-quantitative determination of chemical compositions. Samples for scanning transmission electron microscopy (STEM) were sonicated in methanol for 5 min and then drop cast on AGAR Scientific 400 mesh continuous carbon coated Cu support grids. Elemental mapping was conducted by STEM energy dispersive spectroscopy (STEM-EDS) using a FEI Titan G2 ChemiSTEM operating at 200 kV with 360 pA beam current and the quantification was corrected using the ZAF method. The specific surface area was determined using the nitrogen gas adsorption-desorption method and the Brunauer-Emmer-Teller (BET) model [51] was used to interpret the data. The steady state UV–Vis absorption spectra were recorded using a Cary 5000 UV–Vis–NIR spectrometer. Photoelectrochemical measurements were performed using the conventional three-electrode setup connected to an AUTOLAB PGSTAT 302 N potentiostat-galvanostat. In this configuration we used biomimetic indium sulfide (active area of 1 cm^2) over an adhesive Cu tape as working electrode. Pt wire and an Ag/AgCl electrode were used as the counter and reference electrodes, respectively. The electrolyte was 0.5 M Na_2SO_4 aqueous solution which was deoxygenated by bubbling nitrogen for 10 min before each experiment. A 254 nm UV pen-ray lamp was used as the irradiation source. The decay of the photocurrents was modulated to calculate the transient time constants as described by Fakhouri et al. [52]. For the XPS analysis, the materials were mounted on a piece of Cu tape and analyzed by depth-profiling XPS using synchrotron radiation at the I311 beamline, at the MAX II storage ring at MAX-Lab in Lund Sweden. Survey scans were performed at photon energy of 950 eV. The binding energy of the spectra was calibrated to the C 1s hydrocarbon peak at 284.8 eV. Photon energies were also adjusted to obtain scans of the In 3d and S 2p core levels at fixed kinetic energies (KEs) between 150 and 800 eV in order to vary the sampling depth from 2.9 to 8.9 nm [53]. These were calculated from the inelastic mean free path (IMFP), obtained from the TPP-2M formula, taking the sampling depth to be three times the IMFP [54]. The recorded data were corrected for the different synchrotron flux and photoionization cross sections [55] at different photon energies. Spin-orbit splitting values of 1.1 eV and 7.5 eV [56] between the S $2p_{3/2}$ and S $2p_{1/2}$ multiplets and between In $3d_{3/2}$ and In $3d_{5/2}$ components were used in the peak fitting, respectively, and the full width at half maximum (FWHM) was constrained to be the same between samples.

Photocatalytic hydrogen evaluation

The photocatalytic hydrogen production of the indium sulfide samples was evaluated using 4400 μW cm^{-2} of 254 nm radiation provided by a UV pen-ray lamp. Experiments were performed at room temperature as follows: 0.20 g of the sample was added to 200 mL of deionized water in a batch-type reactor. Before the reaction started, nitrogen gas was bubbled for 10 min into the solution to deoxygenate the system. During the whole photocatalytic water splitting process (4 h), the samples were monitored using a TRACE GC ULTRA chromatograph with a thermal conductivity detector (TCD) and the hydrogen production was determined every 30 min.

Results and discussion

Morphology and structure

Fig. 1 shows the XRD pattern of the control and biomimetic indium sulfide. The XRD peaks around 2θ = 27.7°, 33.4°, 43.9° and 47.9° can be indexed to the (311), (400), (511) and (440) planes, respectively, of the cubic spinel structure $In_{2.77}S_4$ with lattice constant a = 10.74 Å consistent with previously reported values (JCPDS 01-088-2495) [57]. No characteristic peaks due to other impurities, such as In_2O_3 phases were observed.

As can be seen, biomimetic indium sulfide (S1, S2 and S3) has the same crystal structure as control indium sulfide (S0). However, a change in the crystallinity of the material was observed when varying the amount of template used in the synthesis. For S1 and S2 all diffraction peaks are narrow and sharp. In contrast, the peaks of S3 (which is the sample with an excess of a template) are broader and less well defined. The average crystal size of biomimetic indium sulfide was estimated using Scherrer's equation [58] to be around 62.8, 59.8 and 28.4 nm (±0.2 nm) for S1, S2 and S3, respectively. This

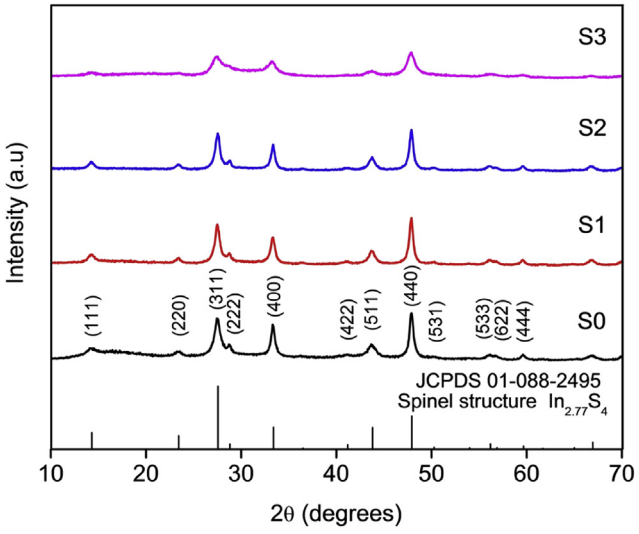

Fig. 1 – XRD patterns of control sample (S0) and biomimetic indium sulfide (S1, S2, S3).

indicates that the average grain size of the biomimetic indium sulfide decreases significantly for the sample with the highest amount of *Mimosa pudica*. S1 and S2 have a similar grain size to S0 (60.2 ± 0.2 nm).

The SEM images in Fig. 2a reveal the morphology of the *Mimosa pudica* leaves used as a template. The leaf powder consists of spherical particles of different diameters in the range 1–3 μm with rough surfaces. The control sample S0 consists of spherical particles built up by many interconnected slightly bending flakes or sheets (consistent in dimension with the microcrystallite size determined by XRD), as shown in Fig. 2b. These microspheres show the 'marigold-like' superstructure characteristic of β-$In_{2.77}S_4$ [59]. The diameter of these particles ranges from less than 1 μm–5 μm. Biomimetic indium sulfide synthesized in the three different ratios (S1, S2 and S3) showed a similar superstructure, but as the amount of template increased, both the size of the microspheres and the size of the individual microcrystallites (as determined by XRD) was reduced (Fig. 2). The particle size of S2 is similar to the original *Mimosa pudica* powder particles. The STEM images in Fig. 3a and b shows the 'marigold-like' microspheres of samples S0 and S2, respectively. It can also be seen that the flakes that compose the microspheres are slightly smaller in the sample with template than in the control sample. In addition, the high resolution STEM images in the insets show interplanar distances corresponding to the (400) and (111) planes of the cubic spinel structure of β-$In_{2.77}S_4$ consistent with the structure observed by XRD. The In/S ratios obtained both by SEM-EDS and STEM-EDS analysis are in agreement with the stoichiometry of the $In_{2.77}S_4$ phase (In:S = 1:1.44), but greater amounts of sulfur were found in the templated sample. Trace amounts of Fe were also detected by STEM-EDS in sample S2 (about 1 atomic percent). This was evenly distributed over the sample, with particle sizes of a few nanometers, as mapped in Fig. 3b. These results, along with the atomic ratios obtained by the XPS analysis (section 3.4) are summarized in Table 1.

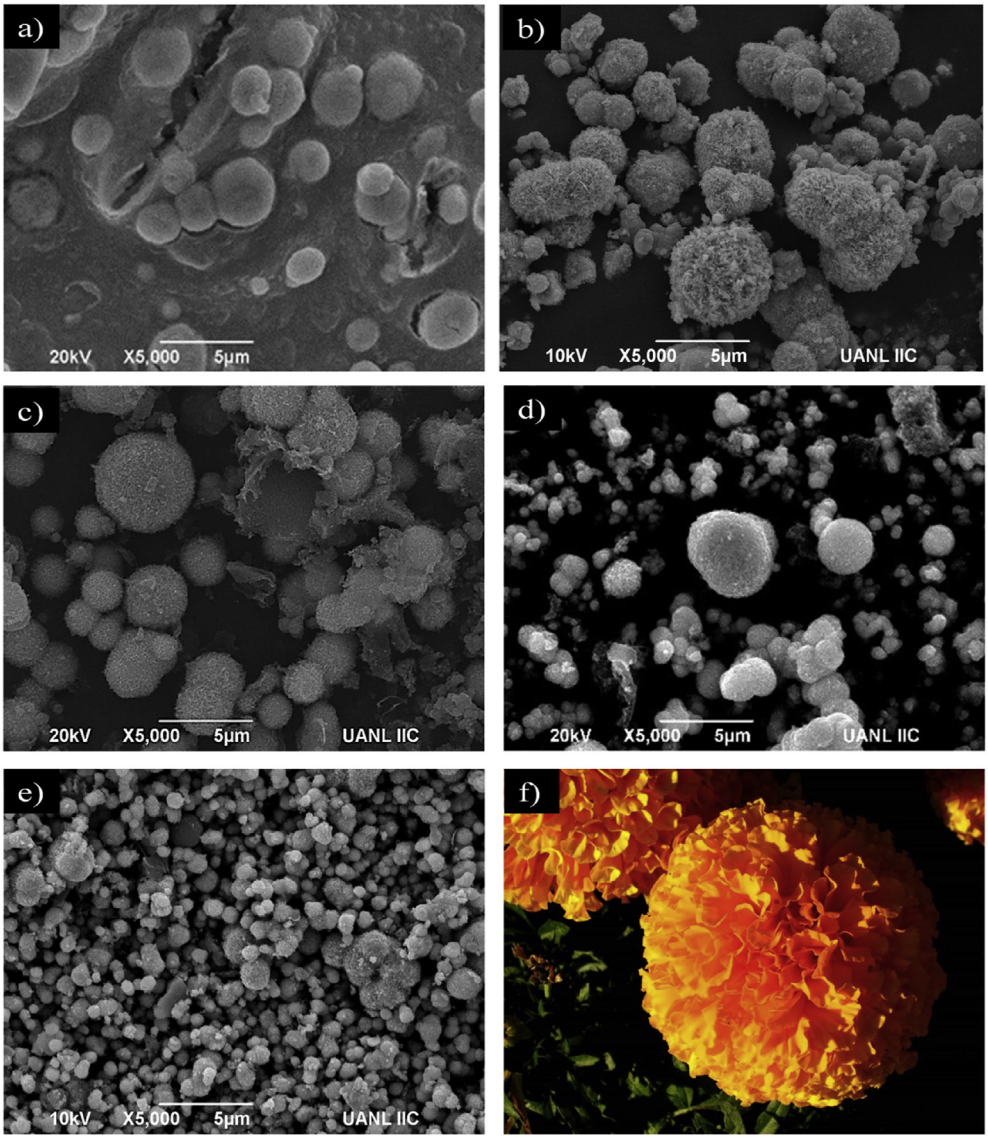

Fig. 2 – SEM images of the samples; a) *Mimosa pudica* leaves; b) S0; c) S1; d) S2; e) S3 and f) marigold flower.

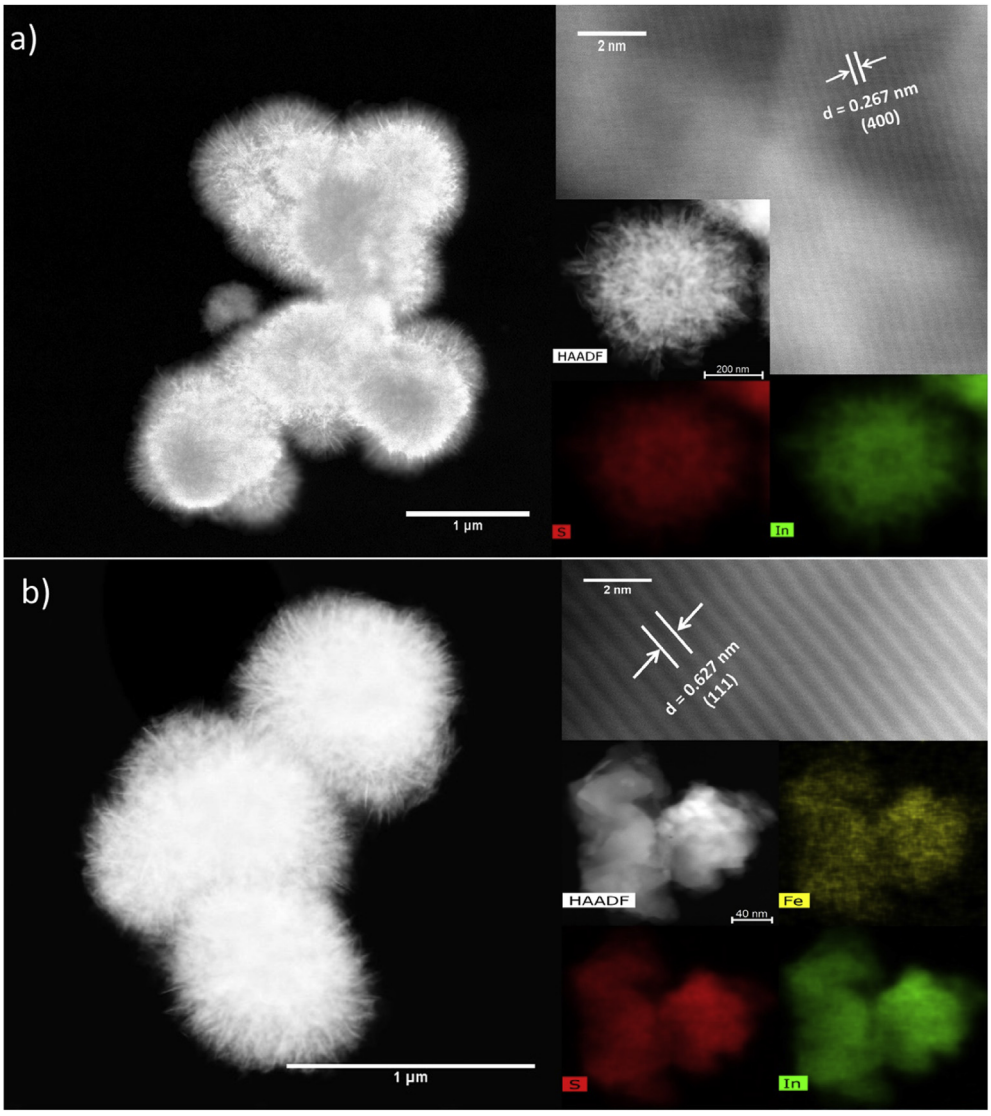

Fig. 3 – STEM images of the samples; a) S0 and b) S2.The high resolution-STEM images show interplanar distances of 0.267 nm and 0.627 nm corresponding respectively to the (400) and (111) planes of cubic β-$In_{2.77}S_4$. Elemental mapping by STEM-EDS shows the presence of Fe only in the biomimetic sample (S2).

The particle size and morphology also have an effect on determining the surface area of the samples; the BET surface area, total pore volume and pore diameter obtained for S2 and the control sample (S0) are shown in Table 1. It is noteworthy that besides a larger surface area, S2 has smaller pore diameter but a larger pore volume density than S0. This implies that S2 contains a higher density of smaller pores than S0, which is likely to lead to an increase in the overall number of active sites. Thus is expected that in S2 a larger number of active sites will be present with a larger volume for the transport of reactants and products, both of which can improve the photocatalytic activity [59,60]. Overall, the effect of the template on the morphology is to decrease the size of the microcrystallite (as shown by XRD), decrease the size of

Table 1 – Atomic ratios obtained by SEM-EDS, STEM-EDS and XPS as well as the BET surface area, pore volume and pore diameter obtained from the nitrogen gas absorption-desorption method for samples S0 and S2.

Sample ID	SEM-EDS In:S:Fe (±0.1)	STEM-EDS In:S:Fe (±0.05)	XPS In:S:Fe (±0.1)	S_{BET} (±0.1 $m^2\ g^{-1}$)	V_{pore} [a] (±0.01 $cm^3\ g^{-1}$)	P_{diam} (±0.1 nm)
S0	1.0:1.5:0.0	1.00:1.59:0.00	1.0:1.0:0.0	19.2	0.10	22.1
S2	1.0:1.7:0.0	1.00:1.63:0.01	1.0:1.3:0.9	69.3	0.16	10.4

[a] The total pore volume density was taken from the N_2 volume adsorbed at $P/P_0 = 0.990$.

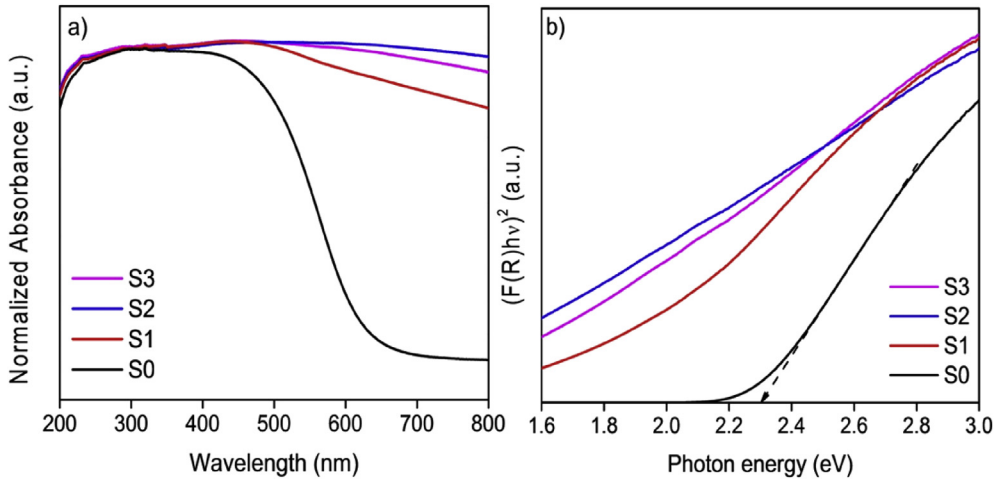

Fig. 4 – a) UV–Vis absorption spectra of control sample (S0) and biomimetic indium sulfide (S1, S2, S3); b) Tauc plot showing $(\alpha h\upsilon)^2$ vs. energy for the control sample (S0) and biomimetic indium sulfide (S1, S2, S3), used to estimate effective band gaps.

the microspheres (as shown by SEM and STEM), and to decrease the average pore size, but to increase their density (as shown by BET measurements).

Optical characterization

The UV–Vis absorption spectra of all the samples are shown in Fig. 4a. It can be observed that for the control sample (S0), the absorbance is at its maximum from ~230 to ~420 nm with an absorption edge at ~540 nm, after which absorption decreases at wavelengths longer than 600 nm. On the other hand, biomimetic indium sulfide showed a higher absorption in the range between ~230 and ~800 nm, i.e. from the UV–vis to the near infrared parts of the solar spectrum. This indicates that biomimetic indium sulfide is more effective in absorbing the solar spectrum than the untemplated semiconductor.

The optical band gap (E_g) of the untemplated indium sulfide was calculated using Tauc's formula [61].

$$\alpha h\upsilon = A(h\upsilon - E_g)^n, \quad (1)$$

where α is the absorption coefficient, h is Planck's constant, A is a proportionality constant, υ is the frequency of the vibration calculated by $\upsilon = c/\lambda$ (where c is the velocity of light and λ is the wavelength obtained from the spectra), and the value of n is taken to be 2, appropriate to a semiconductor with an indirect band gap. The Kubelka-Munk function (F(R)) allows the optical absorbance to be approximated from its reflectance, which is proportional to the absorption coefficient. Thus, α is substituted with F(R) in Tauc's formula.

Fig. 4b shows the plot of $(F(R)h\upsilon)^2$ vs photon energy (eV). Extrapolation of this line to the photon energy axis gives the semiconductor band gap for the untemplated sample to be 2.30 ± 0.01, eV, consistent with previous observations [62]. Band gaps for the templated samples cannot be estimated reliably due the strong absorption in the visible part of the spectrum which we attribute to residual organic matter from the template (probed in more detail by XPS in section 3.4). A similar behavior has been observed in surface-complex-assisted sensitization of TiO_2, used to make it active under visible light illumination [63]. Although the presence of organic compounds does not change the band gap energy values of $In_{2.77}S_4$, their absorption in the visible and near infrared regions could be beneficial for the photocatalytic efficiency if the energy levels are favorably positioned for charge transfer as in dye-sensitized devices. The absorption edges

Table 2 – Binding energies of the assigned S $2p_{3/2}$ components compared with literature values [56,70,71].

Assignment S $2p_{3/2}$	Literature binding energy (eV)	Binding energies found in this work (±0.1 eV)
In_2S_3	161.8 [56,70]	161.7
$-SO_2$	163.9 [70,71]	163.4
SO_3^{2-}	167.1 [70,71]	166.8
SO_4^{2-}	168.8 [70,71]	169.0
S–O/S–C/S–H	162.3/162.0/162.2 [71]	162.5

Table 3 – Binding energies of the assigned In $3d_{5/2}$ components compared with literature values [56,70,73,74].

Assignment In $3d_{5/2}$	Literature binding energy (eV)	Binding energies found in this work (±0.1 eV)
In_2S_3	445.6 [56]	445.5
$In(OH)_xO_y$	446.0 [73]	446.3
$In(OH)_3$	445.0 [70]	–
In_2O_3	444.3 [56]	–
$In(C_5H_7O_2)_3$	445.6 [74]	–
[a]$InPO_4$	445.7 [56]	–
[a]$In(PO_3)_3$	445.7 [56]	–
[a]$In(PO_3)_4$	446.0 [56]	–

[a] No values of binding energy for the In 3d components in indium (III) sulfite $In_2(SO_3)_3$ and indium (III) sulfate $In_2(SO_4)_3$ were found in the literature, so values for phosphates are shown instead since they are likely to be similar.

Table 4 – Summarized photocatalytic activity of biomimetic indium sulfide.

Sample	Crystal size (±0.2 nm)	E_g (*) (±0.01eV)	H_2 produced (±0.2 μmol g^{-1})	H_2 rate (±0.2 μmol g h^{-1})	Time constants (s)	QE (%)
S0	60.2	2.30	22.0	5.5	1.92	1.63
S0 – 0.1%Fe	–	–	34.2	8.6	–	2.54
S0 – 1%Fe	–	–	6.7	1.7	–	0.50
S1	62.8	1.82*	51.7	12.9	6.25	3.83
S2	59.8	1.24*	73.0	18.3	41.6	5.42
S3	28.4	1.46*	46.8	11.7	4.07	3.47

* 'Absorption edges' obtained from extrapolations of the Tauc plots (Fig. 4), which we take to reflect the extent of visible light absorption, rather than the true band gap of the semiconducting $In_{2.77}S_4$.

obtained for each templated material are shown along with the hydrogen evolution data in Table 4.

Electrochemical characterization

The transient photocurrent responses of the samples are shown in Fig. 5a. The control sample (S0) shows the highest photocurrent in comparison with the biomimetic samples, indicating a higher rate of photogeneration of charge carriers. Among biomimetic samples, S2 shows the highest photocurrent, while S3 shows the lowest. According to this, the photocurrent intensity decreases when an excess of *Mimosa pudica* is added to the synthesis. Although S0 shows the highest photocurrent amongst all the samples, no signs of charge extraction or accumulation (characterized by a transient peak in the photocurrent [64]) are observed after the light is turned on. This suggest that in the absence of template, charge transfer to the water molecules is overcome by fast electron-hole-pair recombination which is the dominant process due to the slow kinetics of oxidation of water molecules [65].

In contrast with the untemplated control sample (S0), an anodic peak (a sharp peak in photocurrent) can be observed in the response of all biomimetic samples when the light is switched on, followed by an exponential decrease. This is strongly indicative of hole trapping at the surfaces of these samples [64]. This is produced by the separation of electron-hole pairs at the semiconductor/electrolyte interface, when electrons diffuse to the electrode back contact, while holes are extracted by reduced species (hole acceptors) in the electrolyte. The efficient capture of holes by surface states causes an accumulation of photogenerated holes near to the surface. The decrease in photocurrent intensity shortly after the light is turned on is due to recombination of the photogenerated electrons with the accumulated holes at the surface until equilibrium is reached and the photocurrent becomes constant (a steady state is reached). When the light is turned off, the remaining accumulated holes recombine with free electrons causing electrons to be withdrawn from the external circuit, explaining the transient cathodic response (the sharp negative peaks in Fig. 5a [64,66,67]). Thus, for sample S3, the generation rate of electrons under illumination is lower compared to S2. The transient time constants obtained from the modulation of these photocurrent responses are 1.9, 6.2, 41.6 and 4.1 s (±0.1 s), for S0, S1, S2 and S3, respectively. As these depend on the electron-hole recombination rate, longer time constants can indicate to more competitive water splitting reaction rates. We note that the longest electron-hole recombination time is achieved from sample S2.

Overall, the transient photocurrent responses of the samples suggest that fast electron-hole pair recombination occurs in the untemplated sample (S0), competing strongly with the charge-transfer process needed for water oxidation. However, the addition of a template causes pronounced accumulation

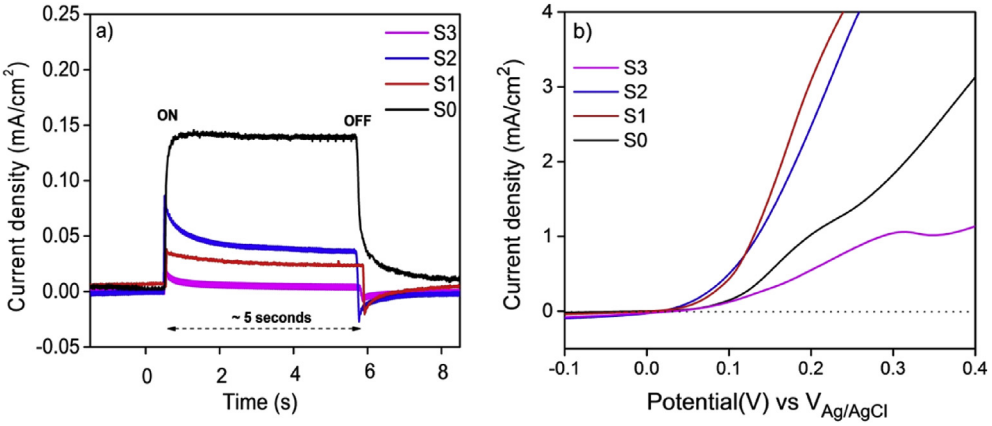

Fig. 5 – a) Photoresponse of control sample (S0) and biomimetic indium sulfide (S1, S2, S3) under 254 nm UV light at open circuit potential (V_{OCP}); b) Linear sweep voltammetry (LSV) characteristic for control sample (S0) and biomimetic indium sulfide (S1, S2, S3) under 254 nm UV light at a sweep rate of 10 mV/s.

of long-lived surface holes, presumably due to the introduction of new surface states. It is therefore important to examine any differences in the surface composition of the samples (section 3.4).

Linear sweep voltammetry (LSV) curves are shown in Fig. 5b. S0 and S3 showed negligible photocurrents at applied potentials below 0.1 V vs Ag/AgCl (onset potential) followed by a slight increase for the former and a plateau (saturation) for the latter, when the applied potential reached 0.3 V vs Ag/AgCl. In contrast, for samples S1 and S2, synthesized with a lower amount of template, a positive change in the onset potential to 0.04 V vs Ag/AgCl and a sharper rise in photocurrent was observed as the applied bias was increased, indicating that these samples exhibit the lowest resistance for the extraction of photogenerated electrons, which could be beneficial for the photocatalytic process [68].

XPS analysis

Comparison of the core level XPS signals of S2 (Fig. 6a) with S0 (Fig. 6b) showed higher relative intensities of In 3d, S 2p and S 2s peaks for the latter relative to C 1s. Peaks from the weaker core level features of In and S, such as In 4d, In $3p_{1/2}$ and In $3p_{3/2}$ spectral lines are also present in the spectrum of S0. In contrast, the spectrum of the sample with template (S2) showed greater amounts of C 1s and O 1s and 2s, as expected from the residual organic matter of the *Mimosa pudica* leaves, and peaks corresponding to the binding energies of N 1s, Fe 2p, 3p and $M_{23}VV$ Auger (see Fig. 5a). Elemental quantification from the peaks in these survey scans gives approximate atomic ratios (ignoring variation in sampling depth with photoelectron KE) of In:S:C:O:Fe as 1.0:1.0:4.5:1.3:0.0 (±0.1) for S0 and 1.0:1.3:41.0:22.4:0.9 (±0.1) for S2. This clearly demonstrates the very large increase in surface C and O in the templated sample, which we associate with residual organic matter form the template. The Fe present in the templated sample is believed to come from the *Mimosa pudica* leaves as a contaminant, since this is a metal found in abundance in Particulate Matter Below 2.5 μm Size ($PM_{2.5}$) air samples of the area originating from the erosion of the naturally iron-rich soil of the region [69]. Moreover, this element is present mainly on the surface of the sample since higher amounts were detected by XPS (which is a much more surface sensitive technique) than by EDS.

The S 2p signals from the samples are shown in Fig. 7. The sample synthesized with a template (S2), shown in Fig. 6a, showed clear signals due to sulfur oxidation products such as sulfur-adsorbed $-SO_2$, SO_3^{2-} and SO_4^{2-} (each below 10% of total S), and organic forms of sulfur species bonding with carbon, oxygen and hydrogen (S–O/S–C/S–H) in amounts between 5 and 15% of the total amount of S probed at each sampling depth [56,70,71]. These species are not present in S0 (Fig. 7b) where all the sulfur present is associated with the indium sulfide phase. Other authors have observed the formation of a sulfate layer, $In_2(SO_4)_3$, at the surface of sulfide materials exposed to oxidizing environments such as O_2 and H_2O [70,72]. The binding energies used from literature for the components fitted in the peak deconvolution of these spectra are given in Table 2. The experimental data are generally in good agreement with the literature values, given the uncertainty in measurement (±0.1 eV).

Fig. 8 shows scans of the In 3d peaks at different kinetic energies (KEs) (and hence sampling depths) for samples with and without the template. The binding energies found in the literature for the components fitted are shown in Table 3. As can be seen in Fig. 8a, additional components at higher binding energies than the In 3d multiplet due to indium sulfide are present at the surface of the S2 sample. These could be characteristic of a hydroxide/oxide phase ($In(OH)_xO_y$) formed by surface oxidation. This phase has been seen as a nucleation phase when growing $In(OH_x)S_y$ by chemical bath deposition (CBD) [73]. We would expect the BEs of other oxidized In species, such as indium (III) sulfite $In_2(SO_3)_3$ and indium (III) sulfate $In_2(SO_4)_3$ to be similar (see Table 3). These features decrease in intensity as the sampling depth increases showing that the bulk material is free of oxidation. In contrast, S0 shows only components corresponding to indium sulfide at all the analyzed depths (see Fig. 8b) and (as for the S 2p peaks) there are no signs of oxidation products or species other than indium sulfide. The slight asymmetry observed in the lower binding energy side of the In $3d_{3/2}$ peak at 150 KE arises from an Auger S MNN feature with a kinetic energy of 152 eV.

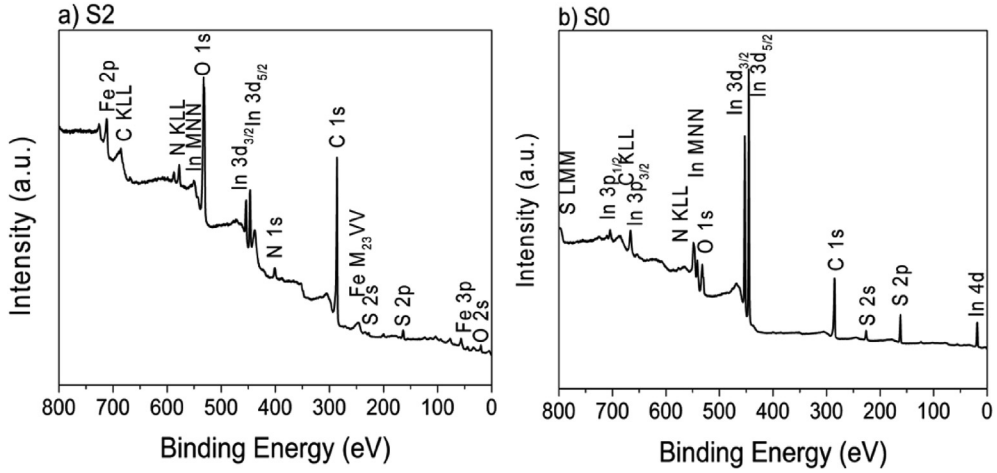

Fig. 6 – Survey scans spectra of indium sulfide samples at photon energy of 950 eV; a) S2, b) S0.

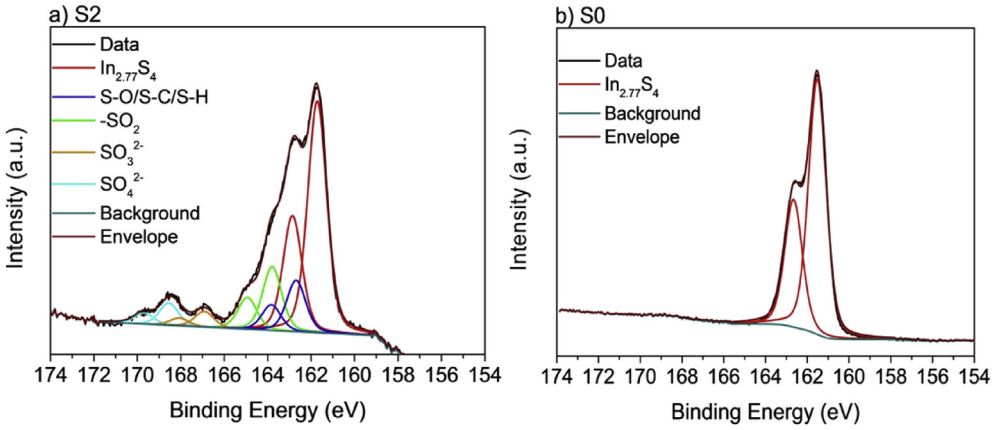

Fig. 7 – Fitted spectra of the S 2p region for the samples showing the fitting of the S $2p_{3/2,1/2}$ multiplet for each chemical component; a) S2, b) S0, at photon energies of 312 and 762 eV, respectively. Note that for clarity in the features shown, the spectra compared in this image were recorded at different photon energies and thus correspond to different sampling depths.

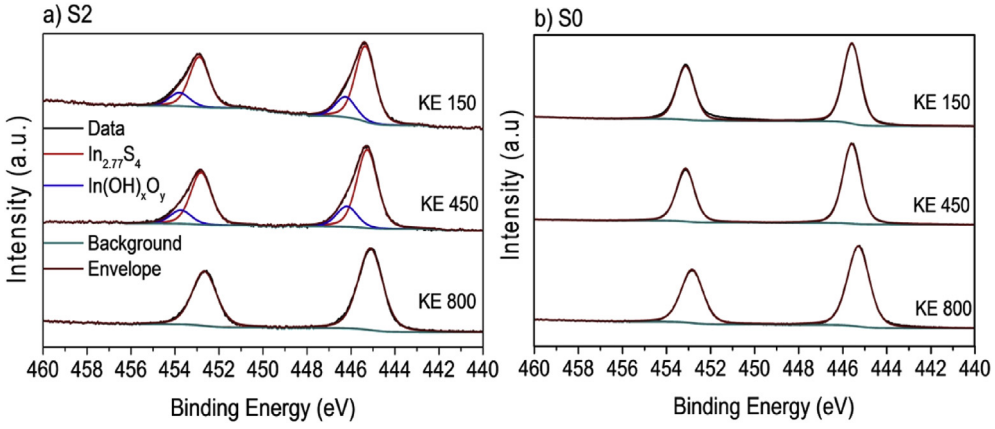

Fig. 8 – Fitted spectra of the In 3d region at 150, 450 and 800 eV kE (sampling depths of 2.9, 5.8 and 8.9 nm, respectively) for the samples; a) S2, b) S0. The fitting of the In $3d_{5/2,\ 3/2}$ multiplet is shown for each chemical component.

Overall, XPS shows significant changes in surface chemistry between the untemplated and templated samples.

Photocatalytic hydrogen production

Fig. 9 shows the photocatalytic hydrogen production of all the samples. As can be seen, the rate of hydrogen production is higher for biomimetic indium sulfide than for the control samples (S0, S0 – 0.1%Fe and S0 – 1%Fe) and the photocatalytic activity increases as the amount of *Mimosa pudica* increases up to a 1:1 ratio (S2) where hydrogen production peaks, decreasing with an excess of template (S3). All values are summarized in Table 4. The apparent quantum efficiency (*QE*) was calculated based on the formula

$$QE(\%) = \frac{2N_{H_2}}{Nh\upsilon}, \quad (2)$$

where N_{H_2} is the number of evolved H_2 molecules and $Nh\upsilon$ is the number of incident photons [75,76], by quantifying the amount of hydrogen at a given incident photon flux. The number of incident photons was calculated as 5.62×10^{15} photons·s^{-1}. The hydrogen production for the S0 sample is 22 μmol g^{-1}, while for S2, the hydrogen production increases sharply to 73 μmol g^{-1}, more than 3 times the value for S0, corresponding to a *QE* of 5.42% at 254 nm. S1 and S3 produced similar amounts of hydrogen and showed practically the same *QE* despite their difference in particle size and hence surface areas. Among the control samples, S0 – 0.1%Fe showed the highest hydrogen production, while S0 – 1%Fe showed the lowest, indicating that the hydrogen production increases with small amounts of Fe but decreases with an excess of it. A similar behavior has been observed for indium sulfide films where the presence of indium oxide in moderate amounts induced efficient charge separation, but the overall activity decreased for higher concentrations [25].

To summarize our observations, the addition of Mimosa pudica leaves as template in the synthesis of indium sulfide has an effect on the morphology, the optical properties and the surface composition of biomimetic indium sulfide. The morphology of the particles plays an important role in its photocatalytic activity. Among the biomimetic indium sulfide samples, sample S2 showed a significantly decreased

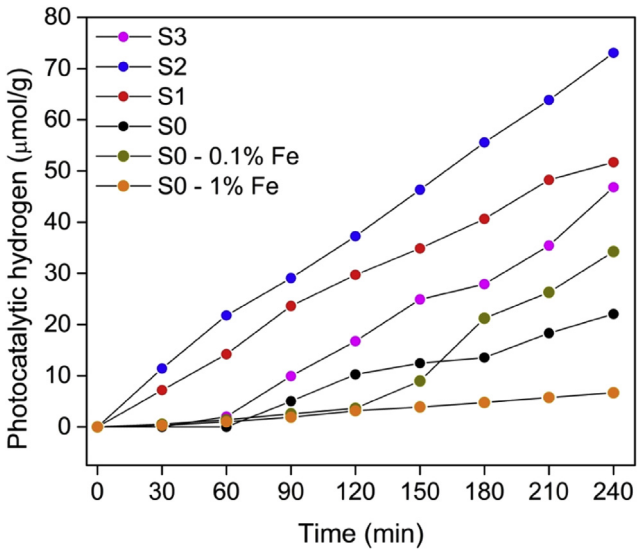

Fig. 9 – Photocatalytic hydrogen production of control samples (S0, S0 - 0.1%Fe and S0 – 1%Fe) and biomimetic indium sulfide (S1, S2, S3).

microsphere size and increased pore volume density and surface area but with a crystallinity (grain size) very close to that of the control (S0). This sample also has the lowest absorption edge energy, indicating a better absorption of the visible part of the solar spectrum. Moreover, its photoelectrochemical performance was superior to that of samples S1 and S3. The photocatalytic activity of samples S2 and S0 in H_2 production scales approximately with their surface areas. This is anticipated, since larger specific surface areas promote a higher charge transfer across the semiconductor enhancing its photocatalytic activity. However, a large surface area may also increase the non-radiative electron-hole pair recombination rate, due to the presence of more recombination sites. In this context, the semiconductor must have an optimal surface area to allow a better charge transfer while keeping low the number of sites where the photogenerated electron-hole pairs can recombine [77]. The fact that S1 and S3 have the same *QE* and similar transient photocurrent time constants (suggesting similar electron-hole recombination times) but clearly (from XRD and SEM) different sizes, and therefore very different surface areas, supports this idea. Further, we note that as the microcrystallite and microsphere size is reduced between S2 and S3 (which we would expect to increase the active area) there is a decrease, not an increase in the rate of photocatalytic H_2 production.

In our case, however, there are also significant changes in surface chemistry accompanying the morphology changes, which are also likely to influence the photocatalytic activity. The XPS analysis revealed that the surface of the biomimetic sample S2 has significantly larger amounts of carbon and organic matter than control sample (S0). Consequently, it may be the case that when an excess of template is used in the synthesis (S3), a deactivation of the photocatalyst by coking, i.e. the interaction of carbon-containing molecules with the active sites in the surface, decreases the photocatalytic activity [78]. Alternatively, although the organic matter from the template clearly improves absorption in the visible part of the spectrum (Fig. 3), the absolute photoabsorption cross section of the underlying semiconductor may eventually be reduced by the thick overlying organic layer as more template is added. Thus we suggest that an optimum photocatalytic behavior is achieved for sample S2 because further increases in the surface area and amount of template cause an increase in the non-radiative recombination rate coupled with a decrease in the availability of active sites and possible reduction in absorption cross section as the thickness of the surface organic layer increases.

In addition to the possible deactivation of the catalyst by the accumulation of a carbon overlayer, we must also consider the effects of the other species identified on the surface. Among the species found on the surface of biomimetic indium sulfide were also Fe (with a binding energy consistent with Fe_2O_3) and sulfur oxidation products such as $-SO_2$, SO_3^{2-} and SO_4^{2-} in significant amounts. Fe_2O_3 is not active for hydrogen production on its own because its conduction band is located under the reduction potential of water [79]. However, its valence band lies well below the water oxidation potential [64,80] and photocatalytic activity has been reported for direct O_2 evolution [81]. Even though both bands of indium sulfide are well positioned for overall water splitting [80] they are more suitable for proton reduction, and therefore the coupling with Fe_2O_3 (more favorable for water oxidation) could improve the charge separation, increasing the hydrogen production rate. This is in agreement with efforts being made to engineer

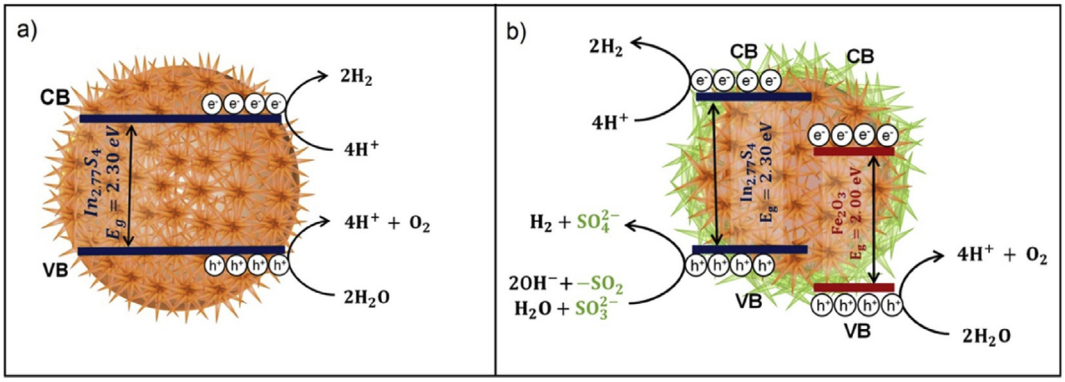

Fig. 10 – Photocatalytic activity diagram of; a) control sample (S0) and b) the biomimetic indium sulfide (S2).

the band alignment of semiconductor heterostructures to promote charge separation reducing recombination rates. Moreover, the accumulation of long-lived holes at surface states described in the electrochemical characterization section has been identified to be fundamental for the water oxidation reaction on Fe_2O_3 surfaces [82]. The results from samples S0 – 0.1%Fe and S0 – 1%Fe have shown that the addition of iron oxide has an effect in the photocatalytic activity of indium sulfide. The activity is enhanced for low Fe concentrations (0.1%) but is reduced when larger amounts of Fe (1%) are added. We suggest that this is due to increasing transfer of electrons into Fe_2O_3 and holes into indium sulfide consistent with the photocatalytic activity diagram in Fig. 10b. Another significant aspect is the presence of partially-oxidized sulfur species ($-SO_2$ and SO_3^{2-}) which are easily oxidizable and could enhance the photocatalytic activity for hydrogen production by acting as sacrificial reagents (electron donors) on the surface of the indium sulfide particles [83]. A summary of these effects is illustrated in Fig. 10.

Conclusions

In this work, biomimetic indium sulfide was synthesized by a template-assisted hydrothermal method using *Mimosa pudica* leaves as template for the first time. As a result, the photocatalytic hydrogen production of the biomimetic indium sulfide was increased. Specifically, biomimetic indium sulfide prepared with 1:1 wt ratio (S2) showed the highest photocatalytic activity reaching 73 $\mu mol \cdot g-1$, which is more than three times the amount produced with indium sulfide without template (S0). This increased activity is correlated with a 20-fold increase in the electron-hole recombination time compared with the sample without the template. This enhanced photocatalytic activity can be attributed to the difference in morphology obtained due to the *Mimosa pudica* template and the chemical species found on the surface of the biomimetic material. The effect of the template on morphology is to decrease the size of the microspheres and the average pore size, but to increase their density. The morphology obtained in biomimetic indium sulfide, is beneficial for light harvesting and electron mobility. Moreover, the surface iron oxide (Fe_2O_3) and sulfur species ($-SO_2$ and SO_3^{2-}) can work as water oxidizer (driven by holes at the surface) and sacrificial electron donors respectively, for photocatalytic water splitting improving the performance for hydrogen production. This strategy provides a new way to synthesize functionalized photocatalysts inspired by nature that can be used in many technological applications.

Acknowledgements

Authors want to thank CONACYT for financial support to the projects CB-237049, CB-256645. Also thank SEP for support for the projects PROFOCIE-2014-19-MSU0011T-18, and Integración de Redes Temáticas 2015-CA-244, as well as FIC-UANL for support for the project PAIFIC-2015. The work at MAX-lab was funded under The European Community's Seventh Framework Programme (FP7/2007–2013) under grant agreement no. 226716 and by EPSRC travel grant EP/H0020446/1. MAL and WRF would like to thank EPSRC for financial support (grant number EP/K008544/1). In addition, the authors want to thank CONACYT for the Master in Science scholarship support for Omar Ali Carrasco Jaim, No. 287841 and PhD scholarship for Ruben Ahumada Lazo No. 284566. S. J. H. acknowledges funding from the European Research Council (Horizon 2020, grant agreement ERC-2016-STG-EvoluTEM-715502). The data associated with this paper are openly available from The University of Manchester eScholar Data Repository: dx.doi.org/10.15127/1.307290.

REFERENCES

[1] Maeda K, Domen K. Photocatalytic water splitting: recent progress and future challenges. J Phys Chem Lett 2010;1:2655–61. https://doi.org/10.1021/jz1007966.
[2] Maeda K. Photocatalytic water splitting using semiconductor particles: history and recent developments. J Photochem Photobiol C Photochem Rev 2011;12:237–68. https://doi.org/10.1016/j.jphotochemrev.2011.07.001.
[3] Fujishima A, Honda K. Electrochemical photolysis of water at a semiconductor electrode. Nature 1972;238:37–8. https://doi.org/10.1038/238037a0.
[4] Janáky C, Rajeshwar K, De Tacconi NR, Chanmanee W, Huda MN. Tungsten-based oxide semiconductors for solar hydrogen generation. Catal Today 2013;199:53–64. https://doi.org/10.1016/j.cattod.2012.07.020.
[5] Chen X, Shen S, Guo L, Mao SS. Semiconductor-based photocatalytic hydrogen generation. Chem Rev 2010;110:6503–70. https://doi.org/10.1021/cr1001645.
[6] Yao X, Liu T, Liu X, Lu L. Loading of CdS nanoparticles on the (101) surface of elongated TiO2 nanocrystals for efficient visible-light photocatalytic hydrogen evolution from water splitting. Chem Eng J 2014;255:28–39. https://doi.org/10.1016/j.cej.2014.06.055.
[7] Bao N, Shen L, Takata T, Domen K. Self-templated synthesis of nanoporous CdS nanostructures for highly efficient photocatalytic hydrogen production under visible light. Chem Mater 2008;20:110–7. https://doi.org/10.1021/cm7029344.
[8] Xu J, Cao X. Characterization and mechanism of MoS2/CdS composite photocatalyst used for hydrogen production from water splitting under visible light. Chem Eng J 2015;260:642–8. https://doi.org/10.1016/j.cej.2014.07.046.
[9] Wang H, Chen W, Zhang J, Huang C, Mao L. Nickel nanoparticles modified CdS - a potential photocatalyst for hydrogen production through water splitting under visible light irradiation. Int J Hydrogen Energy 2015;40:340–5. https://doi.org/10.1016/j.ijhydene.2014.11.005.
[10] Buehler N, Meier K, Reber J. Photochemical hydrogen production with cadmium sulfide suspensions. J Phys Chem 1984:3261–8. https://doi.org/10.1021/j150659a025.
[11] He Y, Li D, Xiao G, Chen W, Chen Y, Sun M, et al. A new application of nanocrystal in 2 S 3 in efficient degradation of organic pollutants under visible light irradiation. J Phys Chem C 2009;113:5254–62. https://doi.org/10.1021/jp809028y.
[12] Wu W, Lin R, Shen L, Liang R, Yuan R, Wu L. Visible-light-induced photocatalytic hydrogenation of 4-nitroaniline over In2S3 photocatalyst in water. Catal Commun 2013;40:1–4. https://doi.org/10.1016/j.catcom.2013.05.016.
[13] Rengaraj S, Venkataraj S, Tai CW, Kim Y, Repo E, Sillanpää M. Self-assembled mesoporous hierarchical-like In2S3 hollow

microspheres composed of nanofibers and nanosheets and their photocatalytic activity. Langmuir 2011;27:5534–41. https://doi.org/10.1021/la104780d.
[14] Ho CH. Growth and characterization of near-band-edge transitions in β-In 2S3 single crystals. J Cryst Growth 2010;312:2718–23. https://doi.org/10.1016/j.jcrysgro.2010.06.018.
[15] Barreau N. Indium sulfide and relatives in the world of photovoltaics. Sol Energy 2009;83:363–71. https://doi.org/10.1016/j.solener.2008.08.008.
[16] Zavrazhnov AY, Kosyakov AV, Naumov AV, Sergeeva AV, Berezin SS. Study of the In-S phase diagram using spectrophotometric characterization of equilibria between hydrogen and indium sulfides. Thermochim Acta 2013;566:169–74. https://doi.org/10.1016/j.tca.2013.05.031.
[17] Shi W, Song S, Zhang H. Hydrothermal synthetic strategies of inorganic semiconducting nanostructures. Chem Soc Rev 2013;42:5714–43. https://doi.org/10.1039/c3cs60012b.
[18] Feng SH, Li GH. Hydrothermal and solvothermal syntheses. 2017. https://doi.org/10.1016/B978-0-444-63591-4.00004-5.
[19] Ou C, Sanchez-Jimenez PE, Datta A, Boughey FL, Whiter RA, Sahonta S-L, et al. Template-assisted hydrothermal growth of aligned zinc oxide nanowires for piezoelectric energy harvesting applications. ACS Appl Mater Interfaces 2016;8:13678–83. https://doi.org/10.1021/acsami.6b04041.
[20] Ghaderi Sheikhi Abadi P, Salavati-Niasari M, Davar F. Hydrothermal synthesis, characterization and optical properties of 3D flower like indium sulfide nanostructures. Superlattice Microst 2013;53:76–88. https://doi.org/10.1016/j.spmi.2012.09.003.
[21] Wu X, Li H, Sun Y, Wang Y, Zhang C, Gong X, et al. One-step hydrothermal synthesis of In2.77S4 nanosheets with efficient photocatalytic activity under visible light. Appl Phys A 2017;123:426. https://doi.org/10.1007/s00339-017-1016-0.
[22] Fu X, Wang X, Chen Z, Zhang Z, Li Z, Leung DYC, et al. Photocatalytic performance of tetragonal and cubic β-In2S3 for the water splitting under visible light irradiation. Appl Catal B Environ 2010;95:393–9. https://doi.org/10.1016/j.apcatb.2010.01.018.
[23] Chen J, Liu W, Gao W. Tuning photocatalytic activity of In2S3 broadband spectrum photocatalyst based on morphology. Appl Surf Sci 2016;368:288–97. https://doi.org/10.1016/j.apsusc.2016.02.008.
[24] Wu X, Li H, Su J, Zhang J, Feng Y. Fabrication and characterization of visible light-driven in 2 . 77 S 4/In (OH) 3 composite photocatalysts with excellent redox performance. 2018.
[25] Feng X, Chen Y, Wang M, Guo L. Hydrothermal synthesis of pyramid-like In2S3film for efficient photoelectrochemical hydrogen generation. Int J Hydrogen Energy 2017;42:15085–95. https://doi.org/10.1016/j.ijhydene.2017.04.283.
[26] Herrmann JM, Disdier J, Pichat P. Effect of chromium doping on the electrical and catalytic properties of powder titania under UV and visible illumination. Chem Phys Lett 1984;108:618–22. https://doi.org/10.1016/0009-2614(84)85067-8.
[27] Marschall R, Wang L. Non-metal doping of transition metal oxides for visible-light photocatalysis. Catal Today 2014;225:111–35. https://doi.org/10.1016/j.cattod.2013.10.088.
[28] Diak M, Grabowska E, Zaleska A. Synthesis, characterization and photocatalytic activity of noble metal-modified TiO2 nanosheets with exposed {001} facets. Appl Surf Sci 2015;347:275–85. https://doi.org/10.1016/j.apsusc.2015.04.103.
[29] Singh AV, Rahman A, Sudhir Kumar NVG, Aditi AS, Galluzzi M, Bovio S, et al. Bio-inspired approaches to design smart fabrics. Mater Des 2012;36:829–39. https://doi.org/10.1016/j.matdes.2011.01.061.
[30] Bar-Cohen Y. Biomimetics–using nature to inspire human innovation. Bioinspiration Biomimetics 2006;1:P1–12. https://doi.org/10.1088/1748-3182/1/1/P01.
[31] Garcia AP, Buehler MJ. Bioinspired nanoporous silicon provides great toughness at great deformability. Comput Mater Sci 2010;48:303–9. https://doi.org/10.1016/j.commatsci.2010.01.011.
[32] Dou L, Gao L, Yang X, Song X. Hierarchical architectures TiO 2: pollen-inducted synthesis, remarkable crystalline-phase stability, tunable size, and reused photo-catalysis. J Hazard Mater 2012;203(204):363–9. https://doi.org/10.1016/j.jhazmat.2011.12.043.
[33] Chen J, Su H, Song F, Moon WJ, Kim YS, Zhang D. Bioinspired Au/TiO 2 photocatalyst derived from butterfly wing (Papilio Paris). J Colloid Interface Sci 2012;370:117–23. https://doi.org/10.1016/j.jcis.2011.12.055.
[34] Ding L, Zhou H, Lou S, Ding J, Zhang D, Zhu H, et al. Butterfly wing architecture assisted CdS/Au/TiO2 Z-scheme type photocatalytic water splitting. Int J Hydrogen Energy 2013;38:8244–53. https://doi.org/10.1016/j.ijhydene.2013.04.093.
[35] Bridoux MC, Keil RG, Ingalls AE. Analysis of natural diatom communities reveals novel insights into the diversity of long chain polyamine (LCPA) structures involved in silica precipitation. Org Geochem 2012;47:9–21. https://doi.org/10.1016/j.orggeochem.2012.02.010.
[36] Zampieri A, Mabande GTP, Selvam T, Schwieger W, Rudolph A, Hermann R, et al. Biotemplating of Luffa cylindrica sponges to self-supporting hierarchical zeolite macrostructures for bio-inspired structured catalytic reactors. Mater Sci Eng C 2006;26:130–5. https://doi.org/10.1016/j.msec.2005.08.036.
[37] Qian J, Cao Y, Chen Z, Liu C, Lu X. Biomimetic synthesis of cerium oxide nanosquares on RGO and their enhanced photocatalytic activities. Dalton Trans 2017;46:547–53. https://doi.org/10.1039/c6dt03375j.
[38] Zhou H, Guo J, Li P, Fan T, Zhang D, Ye J. Leaf-architectured 3D hierarchical artificial photosynthetic system of perovskite titanates towards CO_2 photoreduction into hydrocarbon fuels. Sci Rep 2013;3:1667. https://doi.org/10.1038/srep01667.
[39] Coppens MO. A nature-inspired approach to reactor and catalysis engineering. Curr Opin Chem Eng 2012;1:281–9. https://doi.org/10.1016/j.coche.2012.03.002.
[40] Fondeville JC, Borthwick HA, Hendricks SB. Leaflet movement of Mimosa pudica L. Indicative of phytochrome action. Planta 1966;69:357–64. https://doi.org/10.1007/BF00392286.
[41] Burkholder PR, Pratt R. Leaf-movements of mimosa pudica in relation to the intensity and wave length of the incident radiation. Am J Bot 1936;23:212–20.
[42] Li X, Fan T, Zhou H, Chow SK, Zhang W, Zhang D, et al. Enhanced light-harvesting and photocatalytic properties in morph-TiO 2 from green-leaf biotemplates. Adv Funct Mater 2009;19:45–56. https://doi.org/10.1002/adfm.200800519.
[43] Su B, Gong S, Ma Z, Yap LW, Cheng W. Mimosa-inspired design of a flexible pressure sensor with touch sensitivity. Small 2015;11:1886–91. https://doi.org/10.1002/smll.201403036.
[44] Wong WSY, Li M, Nisbet DR, Craig VSJ, Wang Z, Tricoli A. Mimosa Origami: a nanostructure-enabled directional self-organization regime of materials. Sci Adv 2016;2. https://doi.org/10.1126/sciadv.1600417.
[45] Mapala K, Pattabi M. Mimosa pudica flower extract mediated green synthesis. Nano World J 2017;3:44–50.
[46] Naveen Prasad BS, Padmesh TVN, Uma Suganya KS, Govindaraju K, Ganesh Kumar V, Vijai Anand K. Structural

and optical properties of watersoluble iron nanoparticles using mimosa pudica leaf extract via green route. UPB Sci Bull Ser B Chem Mater Sci 2016;78:176–84.
[47] Fatimah I, Pradita RY, Nurfalinda A. Plant extract mediated of ZnO nanoparticles by using ethanol extract of mimosa pudica leaves and coffee powder. Procedia Eng 2016;148:43–8. https://doi.org/10.1016/j.proeng.2016.06.483.
[48] Basavaraj RB, Nagabhushana H, Prasad BD, Sharma SC, Venkatachalaiah KN. Mimosa pudica mediated praseodymium substituted calcium silicate nanostructures for white LED application. J Alloy Comp 2017;690:730–40. https://doi.org/10.1016/j.jallcom.2016.08.064.
[49] Basavaraj RB, Darshan GP, Prasad BD, Sharma SC, Selvam P, Premkumar, et al. Rapid visualization of latent fingerprints using novelCaSiO3:Sm3+ nanophosphors fabricated via ultrasound route. J Rare Earths 2018. https://doi.org/10.1016/j.jre.2018.04.019.
[50] Singh HP, Sharma S, Sharma SK, Sharma RK. Biogenic synthesis of metal nanocatalysts using Mimosa pudica leaves for efficient reduction of aromatic nitrocompounds. RSC Adv 2014;4:37816–25. https://doi.org/10.1039/c4ra04233f.
[51] Lowell S, Shields JE, Thomas MA, Thommes M. Characterization of porous solids and powders: surface area, pore size and densitye. Kluwer Academic Publishers; 2004. https://doi.org/10.1007/978-1-4020-2303-3.
[52] Fakhouri H, Arefi-Khonsari F, Jaiswal a K, Pulpytel J. Enhanced visible light photoactivity and charge separation in TiO2/TiN bilayer thin films. Appl Catal Gen 2015;492:83–92. https://doi.org/10.1016/j.apcata.2014.12.030.
[53] Clark PCJ, Radtke H, Pengpad A, Williamson AI, Spencer BF, Hardman JO, et al. The passivating effect of cadmium in PbS/CdS colloidal quantum dot solar cells probed by nm-scale depth profiling. Nanoscale 2017. https://doi.org/10.1039/C7NR00672A.
[54] National Institute of Standards and Technology. NIST Electron IMFP database. 2010.
[55] WebCrossSections n.d. https://vuo.elettra.eu/services/elements/WebElements.html (accessed September 14, 2015).
[56] NIST X-ray Photoelectron Spectroscopy Database. Meas Serv Div Natl Inst Stand Technol 2012. http://srdata.nist.gov/xps/selEnergyType.aspx. [Accessed 14 September 2015].
[57] Lei S, Tang K, Fang Z, Qi Y, Zheng H. Preparation of manganese indium sulfide urchins in aqueous solution-immiscible organic solvent. Mater Res Bull 2006;41:2325–33. https://doi.org/10.1016/j.materresbull.2006.04.015.
[58] Mote V, Purushotham Y, Dole B. Williamson-Hall analysis in estimation of lattice strain in nanometer-sized ZnO particles. J Theor Appl Phys 2012;6:6. https://doi.org/10.1186/2251-7235-6-6.
[59] Shao L, Li J, Liang X, Xie T, Meng S, Jiang D, et al. Novel β-In 2.77 S 4 nanosheet-assembled hierarchical microspheres: synthesis and high performance for photocatalytic reduction of Cr(VI). RSC Adv 2016;6:18227–34. https://doi.org/10.1039/C5RA26850H.
[60] He K, Zhao C, Zhao G, Han G. Effects of pore size on the photocatalytic activity of mesoporous TiO2 prepared by a sol-gel process. J Sol Gel Sci Technol 2015;75:557–63. https://doi.org/10.1007/s10971-015-3726-0.
[61] Guo X, Chen Y, Qin Z, Wang M, Guo L. One-step hydrothermal synthesis of ZnxCd1−xS/ZnO heterostructures for efficient photocatalytic hydrogen production. Int J Hydrogen Energy 2016;41:15208–17. https://doi.org/10.1016/j.ijhydene.2016.05.218.
[62] Abou-Ras D, Kostorz G, Hariskos D, Menner R, Powalla M, Schorr S, et al. Structural and chemical analyses of sputtered InxSy buffer layers in Cu(In,Ga)Se2 thin-film solar cells. Thin Solid Films 2009;517:2792–8. https://doi.org/10.1016/j.tsf.2008.10.138.
[63] Rehman S, Ullah R, Butt AM, Gohar ND. Strategies of making TiO2 and ZnO visible light active. J Hazard Mater 2009;170:560–9. https://doi.org/10.1016/j.jhazmat.2009.05.064.
[64] Peter LM, Wijayantha KGU, Tahir AA. Kinetics of light-driven oxygen evolution at alpha-Fe2O3 electrodes. Faraday Discuss 2012;155:309–22. https://doi.org/10.1039/c1fd00079a.
[65] Tang J, Durrant JR, Klug DR. Mechanism of photocatalytic water splitting in TiO . Reaction of water with photoholes , importance of charge Carrier dynamics , and evidence for four-hole chemistry mechanism of photocatalytic water splitting in TiO 2 . Reaction of water with photoholes. Water 2008;127:13885–91. https://doi.org/10.1021/ja8034637.
[66] Formal F Le, Sivula K, Gra M. The transient photocurrent and photovoltage behavior of a hematite photoanode under working conditions and the influence of surface treatments. J Phys Chem C 2012;116:26707–20.
[67] Dai G, Yu J, Liu G. Synthesis and enhanced visible-light photoelectrocatalytic activity of p– n junction BiOI/TiO2 nanotube arrays. J Phys Chem C 2011;115:7339–46. https://doi.org/10.1021/jp200788n.
[68] Yan J, Li X, Yang S, Wang X, Zhou W, Fang Y, et al. Design and preparation of CdS/H-3D-TiO2/Pt-wire photocatalysis system with enhanced visible-light driven H2 evolution. Int J Hydrogen Energy 2016:1–10. https://doi.org/10.1016/j.ijhydene.2016.08.188.
[69] Badillo-Castañeda CT, Garza-Ocañas L, Garza-Ulloa MCH, Zanatta-Calderón MT, Caballero-Quintero A. Heavy metal content in PM $_{2.5}$ air samples collected in the metropolitan area of monterrey. México. Hum Ecol Risk Assess An Int J 2015;21:2022–35. https://doi.org/10.1080/10807039.2015.1017873.
[70] Bayon R, Maffiotte C, Herrero J. Chemical bath deposition of indium hydroxy sulphide thin films: preparation and XPS characterization. Thin Solid Films 1999;353:100–7.
[71] Cant DJH, Syres KL, Lunt PJB, Radtke H, Treacy J, Thomas PJ, et al. Surface properties of nanocrystalline PbS films deposited at the water-oil interface: a study of atmospheric aging. Langmuir 2015;31:1445–53. https://doi.org/10.1021/la504779h.
[72] Lichtman D, Craig JH, Sailer V, Drinkwine M. AES and XPS spectra of sulfur in sulfur compounds. Appl Surf Sci 1981;7:325–31. https://doi.org/10.1016/0378-5963(81)90080-5.
[73] Kaufmann C, Dobson PJ, Neve S, Bohne W, Klaer J, Klenk R, et al. Growth analysis of chemical bath deposited In(OH)xSy films as buffer layers or CulnS2 thin film solar cells. 2000. p. 688–91.
[74] McGuire GE, Schweitzer GK, Carlson TA. Study of core electron binding energies in some group IIIa, Vb, and VIb compounds. Inorg Chem 1973;12:2450–3. https://doi.org/10.1021/ic50128a045.
[75] Kalisman P, Nakibli Y, Amirav L. Perfect photon-to-hydrogen conversion efficiency. Nano Lett 2016;16:1776–81. https://doi.org/10.1021/acs.nanolett.5b04813.
[76] Yan H, Yang J, Ma G, Wu G, Zong X, Lei Z, et al. Visible-light-driven hydrogen production with extremely high quantum efficiency on Pt-PdS/CdS photocatalyst. J Catal 2009;266:165–8. https://doi.org/10.1016/j.jcat.2009.06.024.
[77] Tuysuz, Harun Chan CK. Solar energy for fuels, vol. 371. Switzerland: Springer International Publishing; 2016. https://doi.org/10.1007/978-3-319-23099-3.
[78] Wolf EE, Alfani F. Catalysts deactivation by coking. Catal Rev 1982;24:329–71. https://doi.org/10.1080/03602458208079657.
[79] Jang JS, Kim HG, Reddy VR, Bae SW, Ji SM, Lee JS. Photocatalytic water splitting over iron oxide nanoparticles intercalated in HTiNb(Ta)O5 layered compounds. J Catal 2005;231:213–22. https://doi.org/10.1016/j.jcat.2005.01.026.

[80] Xu Y, Schoonen MAA. The absolute energy positions of conduction and valence bands of selected semiconducting minerals. Am Mineral 2000;85:543–56. https://doi.org/10.2138/am-2000-0416.

[81] Townsend TK, Sabio EM, Browning ND, Osterloh FE. Photocatalytic water oxidation with suspended alpha-Fe2O3 particles-effects of nanoscaling. Energy Environ Sci 2011;4:4270. https://doi.org/10.1039/c1ee02110a.

[82] Shen S, Lindley SA, Chen X, Zhang JZ. Hematite heterostructures for photoelectrochemical water splitting: rational materials design and charge Carrier dynamics. Energy Environ Sci 2016;9:2744–75. https://doi.org/10.1039/C6EE01845A.

[83] Schneider J, Bahnemann DW. Undesired role of sacrificial reagents in photocatalysis. J Phys Chem Lett 2013;4:3479–83. https://doi.org/10.1021/jz4018199.